Commensurability oscillations in one-dimensional graphene superlattices

Martin Drienovsky,[1] Jonas Joachimsmeyer,[1] Andreas Sandner,[1] Ming-Hao Liu (劉明豪),[2,3]
Takashi Taniguchi,[4] Kenji Watanabe,[4] Klaus Richter,[3] Dieter Weiss,[1] and Jonathan Eroms[1,*]

[1]*Institute of Experimental and Applied Physics, University of Regensburg, D-93040 Regensburg, Germany*
[2]*Department of Physics, National Cheng Kung University, Tainan 70101, Taiwan*
[3]*Institute of Theoretical Physics, University of Regensburg, D-93040 Regensburg, Germany*
[4]*National Institute for Materials Science, 1-1 Namiki, Tsukuba 305-0044, Japan*

(Dated: February 2, 2018)

We report the experimental observation of commensurability oscillations (COs) in 1D graphene superlattices. The widely tunable periodic potential modulation in hBN encapsulated graphene is generated via the interplay of nanopatterned few layer graphene acting as a local bottom gate and a global Si back gate. The longitudinal magneto-resistance shows pronounced COs, when the sample is tuned into the unipolar transport regime. We observe up to six CO minima, providing evidence for a long mean free path despite the potential modulation. Comparison to existing theories shows that small angle scattering is dominant in hBN/graphene/hBN heterostructures. We observe robust COs persisting to temperature exceeding $T = 150$ K. At high temperatures, we find deviations from the predicted T-dependence, which we ascribe to electron-electron scattering.

Due to its high intrinsic mobility, graphene is an ideal material for exploring ballistic phenomena. Charge carrier scattering in graphene at low temperatures is mainly caused by substrate impurities [1], and therefore suspended graphene [2, 3], or graphene-hexagonal boron nitride (hBN) heterostructures [4, 5] were employed to demonstrate a number of effects requiring high mobility. This enabled the observation of the symmetry broken integer quantum Hall effect [6], and the fractional quantum Hall effect [7, 8], including the elusive even-denominator states [9]. Conductance quantization was achieved in suspended graphene [10] and encapsulated graphene [11]. Magnetic focusing was demonstrated in graphene [12], also in the presence of a moiré lattice in a graphene/hBN heterostructure [13]. Local gating of graphene samples allowed the measurement of pronounced Fabry-Pérot resonances [14], electron-optical guiding [15], or Veselago lensing [16]. Following the prediction by Hofstadter, who considered a two-dimensional superlattice exposed to a magnetic field [17], the moiré lattice in graphene/hBN heterostructures led to evidence of this peculiar band structure [18–20]. Also, in high-mobility graphene antidot lattices, where the conductive graphene sheet is perforated by a two-dimensional array of holes, pronounced magnetoresistance peaks have been observed recently [21, 22].

Thus it is surprising that one of the first ballistic effects reported in semiconductor-based two-dimensional electron gases (2DEG), commensurability oscillations in the magnetoresistance caused by a 1D superlattice [23], eluded experimental observation in graphene so far. The reason for that is the challenging task of combining high mobility graphene and a weak nanometer scale periodic potential. When such a weak, 1D superlattice potential is imposed, a 2DEG exhibits distinct $1/B$-periodic oscillations of the longitudinal magnetoresistance R_{xx}, first observed by Weiss *et al.* in GaAs-based heterostructures [23], known as Weiss- or commensurability oscillations (CO). The weak periodic potential leads to an oscillating modulation broadening of the Landau bands which depends on both, magnetic field strength and energy [24, 25]. Minima in R_{xx} are found whenever the Landau bandwidth vanishes, *i.e.* when the bands become flat. In the semi-classical limit of high quantum numbers, this occurs, when the cyclotron diameter $2r_C$ is commensurate with the lattice period a, through [23]

$$2r_C = \left(\lambda - \frac{1}{4}\right) a. \tag{1}$$

Here $r_C = \hbar\sqrt{4\pi n/(g_s g_v)}/eB$, λ a positive integer, n the electron density and g_s (g_v) the spin (valley) degeneracy. In the semi-classical picture [26], the cyclotron motion is subject to an $\vec{E} \times \vec{B}$-drift, yielding the same analytical results.

The commensurability condition Eq. (1) also holds in the case of graphene [27, 28]. What is different, though, is the Landau level spectrum which is equidistant in the case of a conventional 2DEG but has a square root dependence in case of the Dirac fermions in graphene [29, 30]. This has been predicted to also modify the COs [27, 28]. Notably, Matulis and Peeters calculated very robust COs in the quasiclassical region of small fields that should persist up to high temperatures [27].

Here we employ a novel backgating scheme to demonstrate clear cut COs of both Dirac electrons and holes in high-mobility graphene, subjected to a weak unidirectional periodic potential. As the usual technique of placing a metallic grating with nanoscale periodicity fails due to the poor adhesion of metal to the atomically smooth and inert hBN surface we resort to including a patterned bottom gate (PBG) consisting of few layer graphene (FLG) carrying the desired superlattice pattern into the usual van-der-Waals stacking and edge-contacting technique [5]. The hBN/graphene/hBN stack is assembled on top of the PBG. Importantly, the bottom hBN layer has to be kept very thin (< 15 nm) to impose the periodic potential effectively onto the unpatterned graphene sheet For the PBG, we exfoliated a FLG sheet (3-4 layers) onto an oxidized, highly p-doped silicon wafer which served as a uniform global back gate in the measurements. The FLG sheet was patterned into the desired shape by electron beam lithography and oxygen plasma etching. This approach exploits the

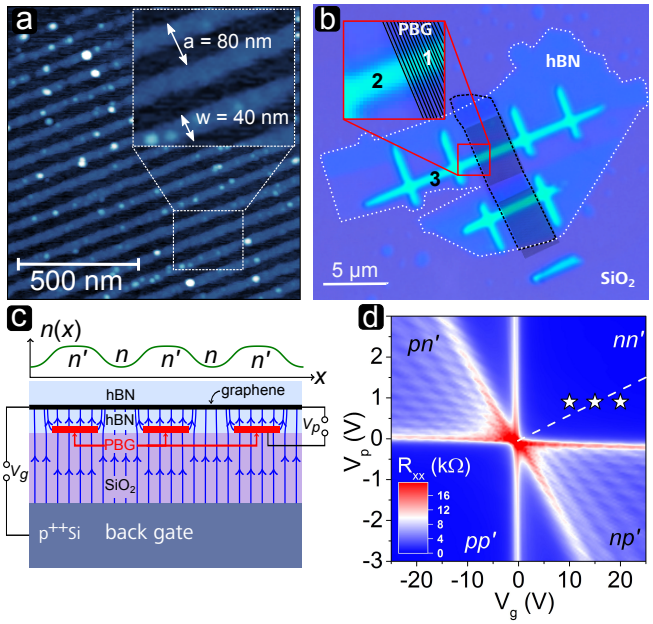

FIG. 1. **Sample geometry and characteristics. a)** AFM image of the PBG of sample B. **b)** hBN/graphene/hBN heterostructure on top of a few layer graphene patterned bottom gate (Sample B, PBG outlined in black, lower hBN outlined in white). Labels 1, 2 and 3 denote the modulated, the unmodulated and the reference area, respectively, see text. **c)** Schematic longitudinal section of the sample geometry, showing the influence of the two independent gates on the graphene charge carrier density in the case of a unipolar modulation. **d)** Resistance map of sample A as a function of gate voltages, V_p (PBG) and V_g (backgate) at $B = 0$. The highly regular Fabry-Pérot pattern in the bipolar regions confirms the presence of identical barriers, forming a superlattice. The white dashed line in the nn'-quadrant represents the $n = n'$-configuration of the two independent gates. The configurations, marked by stars, will be addressed in the text and Fig. 2.

atomic flatness of FLG, which makes it a perfect gate electrode for 2D-material hetrostructures that can be easily etched into various shapes, e.g. 1D or 2D superlattices, split gates, collimators [31] or lenses [32], and allows for nanoscale manipulation of the carrier density. Figure 1**a** shows the AFM image of an 80 nm-stripe lattice used for fabrication of sample B, discussed below. The hBN/graphene/hBN stack was deposited onto the PBG, and a mesa was defined by reactive ion etching (Fig. 1**b**). We used a sequential etching method, employing SF_6 [33], O_2 and CHF_3/O_2-processes, in order to avoid damage to the thin hBN bottom layer covering the PBG (see supplementary material for details). Edge contacts of evaporated Cr/Au (1 nm/ 90 nm) were deposited after reactive ion etching of the contact region and a brief exposure to oxygen plasma. More details on the fabrication are reported elsewhere [34].

The combined action of PBG and the global gate is sketched in Fig. 1**c**. The PBG partially screens the electric field lines emerging from the Si back gate. The latter therefore controls the carrier type and density in the regions between stripes (labeled n), whereas the PBG itself controls primarily those directly above the stripes (labeled n'). A typical charge carrier density profile for a weak potential modulation in the unipolar transport regime is shown atop. Hence, tuning both gates separately we can generate unipolar or bipolar potential modulation on the nanoscale.

Transport measurements were performed in a helium cryostat at temperatures between 1.4 K and 200 K and in perpendicular magnetic fields between 0 to 10 T using low frequency lock-in techniques at a bias current of 10 nA. We present data from two samples (A and B) with a 1D-superlattice period of $a_A = 200$ nm and $a_B = 80$ nm, respectively. The PBGs of both samples, A and B, consist of 19 and 40 few layer graphene stripes, respectively. The thicknesses of the lower hBN, separating the graphene from the PBG are $t_A = 13$ nm and $t_B = 2$ nm, respectively, measured with AFM. Fig. 1**d** displays the zero field resistance of sample A. Using both gates, we can tune into the unipolar regime of comparatively low resistance (labeled nn' and pp') as well as into the bipolar regime (labeled pn' and np'), where pronounced Fabry-Pérot oscillations appear [14, 34–37]. Their regular shape prove the high quality and uniformity of the superlattice potential.

Below, we focus on the unipolar regime, to obtain a weak and tunable 1D superlattice. This is the regime of the COs outlined above. Let us first discuss magnetotransport in sample A with mobility $\mu \approx 130\,000\,\mathrm{cm}^2/\mathrm{Vs}$. In Fig. 2**a-c** we show three magnetic field sweeps, where we keep the PBG-voltage fixed at $V_p = 0.9$ V and tune the modulation strength by varying the backgate voltage V_g. The sweeps represent three different situations, **(a)** $n < n'$, **(b)** $n \approx n'$ and **(c)** $n > n'$. The corresponding V_g, V_p-positions of the sweeps **a**-**c** are marked by stars in the nn'-quadrant of Fig. 1**d**. Moreover, the inset in Fig. 2**b** shows the corresponding charge carrier density profiles that were calculated employing a 1D electrostatic model of the device, including a quantum capacitance correction [36, 38].

In Fig. 2**a** a weak, unipolar ($n < n'$) potential modulation is shown where the longitudinal resistance R_{xx} exhibits well pronounced peaks and dips prior to the emergence of Shubnikov-de-Haas-oscillations (SdHOs), appearing at slightly higher B-fields. The average charge carrier density, extracted from SdHOs is $1.0 \times 10^{12}\,\mathrm{cm}^{-2}$ for this particular gate configuration, yielding a mean free path $l_f = \hbar k_F \mu / e = 1.5\,\mu$m. The expected flat band positions (Eq. (1)), are denoted by the blue vertical dotted lines, perfectly describing the experimentally observed minima. The dips are resolved up to $\lambda = 3$, corresponding to a cyclotron orbit circumference of $2\pi r_C = 1.7\,\mu$m. This clearly confirms that ballistic transport is maintained over many periods of the superlattice.

At $V_g = 15$ V (Fig. 2**b**), $n \approx n'$ holds (see inset Fig. 2**b**). We still observe clear SdHOs, but the COs disappeared. The pronounced peak at $\sim \pm 0.16$ T can be attributed to a magneto-size effect related to boundary scattering in ballistic conductors [39, 40] of width W. While in GaAs based 2DEGs, a ratio $W/r_C \approx 0.5$ is found, we extract $W/r_C \approx 1$ in accordance with

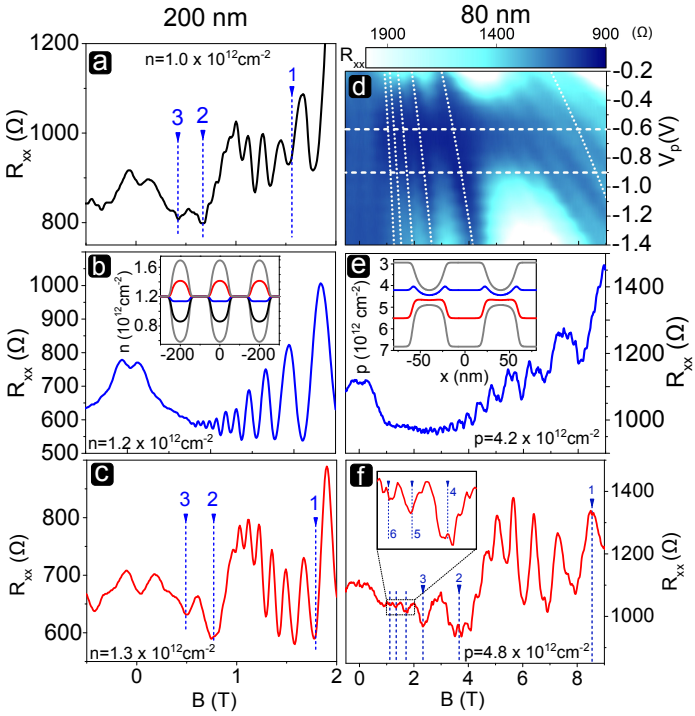

FIG. 2. **Commensurability oscillations in graphene. a-c)** magnetoresistance of sample A ($a_A = 200\,\text{nm}$) at $T = 1.5\,\text{K}$ for fixed $V_p = 0.9\,\text{V}$ and $V_g = 10, 15, 20\,\text{V}$, respectively. The densities n were extracted from SdHOs at higher fields. Vertical blue lines: calculated flat band position (Eq. 1). The COs appear for weak modulation (**a,c**) and disappear in the demodulated situation (**b**). The inset in **b** shows the calculated charge carrier density profiles for blue $V_g = 5...25\,\text{V}$, where situations **a-c** are represented by colors. **d)**: color coded magnetoresistance of sample B ($a = 80\,\text{nm}$), at fixed $V_g = -25\,\text{V}$, $V_p = -0.2\cdots-1.4\,\text{V}$ and $T = 40\,\text{K}$. White dotted lines: guides to the eye for the COs. White dashed lines: sweeps at $T = 1.6\,\text{K}$ shown in **e, f**. **e)**: demodulated configuration. **f)**: minima up to $\lambda = 6$ are resolvable. Inset in **e**: 1D charge carrier density distribution for $V_p = -0.3\cdots-1.2\,\text{V}$, where gate configurations **e,f** are represented by colors.

previous studies on graphene [41].

Further increasing V_g increases n and switches the modulation on again ($n > n'$). The SdHOs in Fig. 2**c** yield an average $n = 1.3\times10^{12}\,\text{cm}^{-2}$. Again, three minima appear at the expected flat band condition described by Eq. (1).

Let us turn to sample B, where we demonstrate COs in the p regime. It has a short period of $a_B = 80\,\text{nm}$ and a bottom hBN flake of only 2 nm thickness, separating the PBG from the graphene. Figure 2**d** shows a color map of the longitudinal resistance as a function of the PBG-voltage V_p and the perpendicular B-field at fixed $V_g = -25\,\text{V}$ (Dirac-point at $V_g = 40\,\text{V}$) and $T = 40\,\text{K}$. Here, the temperature was increased in order to damp the SdHOs for better resolution of the COs. The map shows the B-field response at high average hole densities ($-n = p \approx 4.5\times10^{12}\,\text{cm}^{-2}$). The mobility of $\mu = 45\,000\,\text{cm}^2/\text{Vs}$ and the rather large hole density p give rise to a mean free path $l_f \approx 1.1\,\mu\text{m}$. In the map we can resolve COs up to $\lambda = 6$, corresponding to a cyclotron orbit circumference of $2\pi r_C = 1.4\,\mu\text{m}$, which is comparable to l_f in the average density range considered. The white dotted lines serve as a guide to the eye for the flatband positions.

At around $V_p \sim -0.6\,\text{V}$ the COs disappear as the modulation potential becomes minimal. This is more clearly seen in Fig. 2**e** showing a line cut of Fig. 2**d** at $V_p = -0.6\,\text{V}$ and the corresponding charge carrier density profile in the inset. Here, $p \approx p'$ holds and no COs are resolvable. This changes again at more negative values of $V_p = -0.9\,\text{V}$, shown in Fig. 2**f**, corresponding to the lower line cut in Fig. 2**d**. The calculated flat band conditions using the average hole carrier density of $p = 4.8\times10^{12}\,\text{cm}^{-2}$, extracted from SdHO-minima match perfectly the observed minima. Note that the line cuts in Fig. 2**e,f** were taken at $T = 1.6$ K. The observation of clear cut COs in density modulated hole and electron systems for distinctively different superlattice periods highlights the suitability of graphene PBGs for imposing lateral potentials on graphene films.

As pointed out in the introduction, theory predicted enhanced COs in graphene [27]. To check this and to compare theory and experiment we apply the different prevailing theoretical models to describe $R_{xx}(B)$ for our sample. The amplitude of the COs is governed by the period a, the modulation amplitude V_0 and the Drude transport relaxation time τ_{tr}. Expressions for the additional band conductivity $\Delta\sigma_{yy}$ for 2DEG in [42] and graphene in [27] (Eqs. S1, S9 in supplementary material, respectively), are linear in B and tend to overestimate the CO amplitude at lower field. Mirlin and Wölfle [43] introduced anisotropic scattering to the problem by taking into account the small angle impurity scattering, allowing for a high ratio of the momentum relaxation time τ_{tr} to the elastic scattering time τ_e (Eq. S10, supplementary material). In this approach, both the damping of COs at lower fields and the modulation amplitudes of conventional 2DEGs are correctly described. For the graphene case, Matulis and Peeters employed the Dirac-type Landau level spectrum, as opposed to the parabolic 2DEG situation [27], leading to a modified expression. In their approach, only a single transport scattering time τ_{tr} was included. The temperature dependence of the COs was treated in Refs. [42, 44] for parabolic 2DEGs and in Ref. [27] for graphene. It is expected to exhibit a $x/\sinh(x)$-dependence, where $x = T/T_c$ with the critical temperature

$$T_c = \frac{Bea}{4\pi^2 k_B} v_F. \qquad (2)$$

Here, k_B is the Boltzmann constant and the difference between parabolic and linear dispersion is absorbed in the different Fermi velocities v_F.

To compare to the different theoretical models, we extracted the elastic scattering time $\tau_e = (80\pm10)\,\text{fs}$ from the SdHO-envelope [45] of a reference Hall bar (see supplementary material for details). With $\mu = 45\,000\,\text{cm}^2/\text{Vs}$, we obtain the ratio $\tau_{tr}/\tau_e \approx 11$, which emphasizes the importance of small angle scattering in hBN-encapsulated graphene. The experimental (black) curve in Fig. 3 was taken at $T = 40\,\text{K}$,

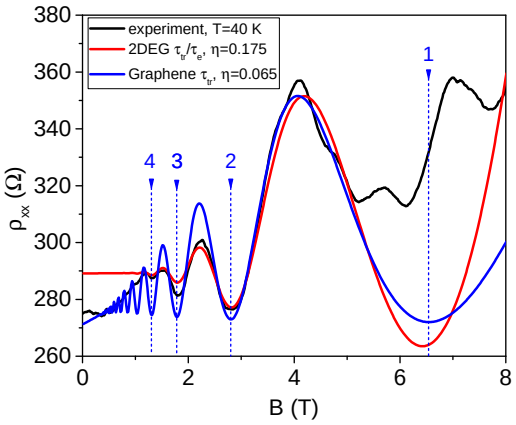

FIG. 3. Comparison of different theoretical expressions with experiment at $V_g = -25\,\mathrm{V}$, $V_p = -0.8\,\mathrm{V}$ and $T = 40\,\mathrm{K}$ (black curve). The blue curve represents the theory for graphene [27] with isotropic scattering and $\eta = 0.065$. The red curve includes small angle impurity scattering [43], using $\eta = 0.175$, matches the experiment well. The experimental curve does not show a pronounced minimum around 6 Tesla due to strong SdHOs setting in.

where the SdHOs are already visibly suppressed, but the amplitude of the COs is practically unchanged, allowing for a better comparison to theory. We first compare our measurement to the graphene theory employing isotropic scattering only. Since the superlattice period $a_B = 80\,\mathrm{nm}$, $\tau_{tr} = 0.9\,\mathrm{ps}$, temperature $T = 40\,\mathrm{K}$ and the average charge carrier density $p = 2.8 \times 10^{12}\,\mathrm{cm}^{-2}$ are known, only $\eta = V_0/E_F$ remains as a fitting parameter. By fitting the theoretical expressions (for details see supplementary material) to the CO peak at ≈ 4 T in Fig. 3 we obtain $\eta = 0.065$. At lower fields, the experimentally observed oscillations decay much faster than the calculated ones. Inserting our sample parameters into the theory employing small angle impurity scattering [43] (Eq. S10, supplementary material), again only $\eta = V_0/E_F$ remains as a free fitting parameter, and we obtain the red trace using $\eta = 0.175$. The fit describes the experimental magnetoresistance strikingly well, although the Dirac nature of the spectrum was not considered. The fits in Fig. 3 imply that including small angle impurity scattering is essential for the correct description of encapsulated graphene.

Finally, we discuss the temperature dependence of COs in 1D modulated graphene. Figure 4**a** depicts a longitudinal resistance trace of sample A at $n = 1.4 \times 10^{12}\,\mathrm{cm}^2$ at different temperatures. The graph clearly demonstrates that the COs are much more robust than the SdHOs. While the latter are almost completely suppressed at $T = 40\,\mathrm{K}$, the COs survive at least up to $T = 150\,\mathrm{K}$ (Sample A) and $T = 200\,\mathrm{K}$ (Sample B), respectively. We analyze the temperature evolution of the first two CO-peaks (marked by red triangles). To determine the peak amplitude, we use the connecting line between two adjacent minima as the bottom line for the evaluation of the peak height [44]. The temperature dependence of the two peaks is

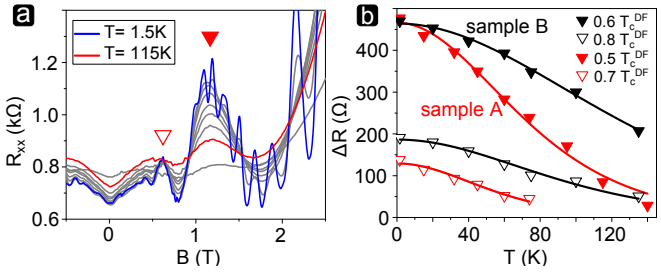

FIG. 4. **Temperature dependence. a)** Longitudinal magnetoresistance of sample A at $V_g = 25\,\mathrm{V}$ and $V_p = 0.9\,\mathrm{V}$ at different temperatures, from 1.5 K to 155 K. **b)** T-dependence of the CO peaks, marked by the red triangles in **a**. The black triangles refer to T-dependence of a similar magnetoresistance trace in sample B. The T-dependence of the peak heights is fitted by $x/\sinh(x)$, where $x = T/T_c$. The extracted critical temperatures T_c are below the expected values for Dirac fermions T_c^{DF}, calculated with Eq. (2).

shown in Fig. 4**b**. Also shown are the corresponding data of sample B (black symbols). We fit the decreasing peak height with $x/\sinh(x)$, *i.e.* the exponential temperature dependence of COs [27, 42, 44], for large $x = T/T_c$, where T_c is the sole fitting parameter. We find consistently lower values for the extracted T_c than predicted by Eq. (2). Tentatively, we attribute this to additional inelastic scattering coming into play at elevated temperatures. For example, it is known that ballistic effects, such as magnetic focusing, are affected by electron-electron scattering even if this does not lead to an enhanced Drude resistance [46]. For hBN encapsulated graphene, this was recently determined to be [47] $\tau_{ee} \sim 0.5\,\mathrm{ps}$ at $T \sim 100\,\mathrm{K}$ and $n = 2 \times 10^{12}\,\mathrm{cm}^{-2}$, *i.e.* somewhat smaller than the transport scattering time in our experiment $\tau_{tr} \sim 0.7\,\mathrm{ps}$ for the same density.

To conclude, we present the first experimental evidence of commensurability oscillations (COs) for both electrons and holes in a hBN-encapsulated monolayer graphene subject to a 1D periodic potential. This was made possible through the combined action of a nanopatterned FLG bottom gate and a global Si back gate. Our approach allows tuning both carrier density and modulation strength independently in a wide range, and on the scale of a few tens of nanometers. The minima in $R_{xx}(B)$ are well described by the flat band condition (1). The predicted strong temperature robustness of COs in graphene was qualitatively confirmed, but detailed comparison to existing theories emphasized the need for a description including anisotropic scattering of charge carriers in encapsulated graphene.

Financial support by the Deutsche Forschungsgemeinschaft (DFG) within the programs GRK 1570 and SFB 689 (projects A7 and A8) and project Ri 681/13 “Ballistic Graphene Devices” is gratefully acknowledged. Growth of hexagonal boron nitride crystals was supported by the Elemental Strategy Initiative conducted by the MEXT, Japan and JSPS KAKENHI Grant Numbers JP15K21722. We thank J. Amann, C. Baumgartner, A. T. Nguyen and J. Sahliger for their contribution towards the optimization of the fabrication procedure.

* jonathan.eroms@ur.de

[1] S. V. Morozov, K. S. Novoselov, M. I. Katsnelson, F. Schedin, D. C. Elias, J. A. Jaszczak, and A. K. Geim, Phys. Rev. Lett. **100**, 016602 (2008).

[2] X. Du, I. Skachko, A. Barker, and E. Y. Andrei, Nature Nanotechnology **3**, 491 (2008).

[3] K. Bolotin, K. Sikes, Z. Jiang, M. Klima, G. Fudenberg, J. Hone, P. Kim, and H. Stormer, Solid State Communications **146**, 351 (2008).

[4] C. R. Dean, A. F. Young, I. Meric, C. Lee, L. Wang, S. Sorgenfrei, K. Watanabe, T. Taniguchi, P. Kim, K. L. Shepard, and J. Hone, Nat. Nanotech. **5**, 722 (2010).

[5] L. Wang, I. Meric, P. Huang, Q. Gao, Y. Gao, H. Tran, T. Taniguchi, K. Watanabe, L. Campos, D. Muller, *et al.*, Science **342**, 614 (2013).

[6] A. F. Young, C. R. Dean, L. Wang, H. Ren, P. Cadden-Zimansky, K. Watanabe, T. Taniguchi, J. Hone, K. L. Shepard, and P. Kim, Nature Physics **8**, 550 (2012).

[7] K. I. Bolotin, F. Ghahari, M. D. Shulman, H. L. Stormer, and P. Kim, Nature **462**, 196 (2009).

[8] X. Du, I. Skachko, F. Duerr, A. Luican, and E. Y. Andrei, Nature **462**, 192 (2009).

[9] J. I. A. Li, C. Tan, S. Chen, Y. Zeng, T. Taniguchi, K. Watanabe, J. Hone, and C. R. Dean, Science **358**, 648 (2017), http://science.sciencemag.org/content/358/6363/648.full.pdf.

[10] N. Tombros, A. Veligura, J. Junesch, M. H. D. Guimaraes, I. J. Vera-Marun, H. T. Jonkman, and B. J. van Wees, Nat Phys **7**, 697 (2011).

[11] B. Terrés, L. A. Chizhova, F. Libisch, J. Peiro, D. Jörger, S. Engels, A. Girschik, K. Watanabe, T. Taniguchi, S. V. Rotkin, J. Burgdörfer, and C. Stampfer, Nature Communications **7**, 11528 (2016).

[12] T. Taychatanapat, K. Watanabe, T. Taniguchi, and P. Jarillo-Herrero, Nature Physics **9**, 225 (2013).

[13] M. Lee, J. R. Wallbank, P. Gallagher, K. Watanabe, T. Taniguchi, V. I. Fal'ko, and D. Goldhaber-Gordon, Science **353**, 1526 (2016), http://science.sciencemag.org/content/353/6307/1526.full.pdf.

[14] P. Rickhaus, R. Maurand, M.-H. Liu, M. Weiss, K. Richter, and C. Schönenberger, Nat. Commun. **4**, 2342 (2013).

[15] P. Rickhaus, M.-H. Liu, P. Makk, R. Maurand, S. Hess, S. Zihlmann, M. Weiss, K. Richter, and C. Schönenberger, Nano Letters **15**, 5819 (2015).

[16] G.-H. Lee, G.-H. Park, and H.-J. Lee, Nature Physics **11**, 925 (2015).

[17] D. R. Hofstadter, Physical Review B **14**, 2239 (1976).

[18] C. R. Dean, L. Wang, P. Maher, C. Forsythe, F. Ghahari, Y. Gao, J. Katoch, M. Ishigami, P. Moon, M. Koshino, T. Taniguchi, K. Watanabe, K. L. Shepard, J. Hone, and P. Kim, Nature **497**, 598 (2013).

[19] B. Hunt, J. Sanchez-Yamagishi, A. Young, M. Yankowitz, B. J. LeRoy, K. Watanabe, T. Taniguchi, P. Moon, M. Koshino, P. Jarillo-Herrero, *et al.*, Science **340**, 1427 (2013).

[20] L. A. Ponomarenko, R. V. Gorbachev, G. L. Yu, D. C. Elias, R. Jalil, A. A. Patel, A. Mishchenko, A. S. Mayorov, C. R. Woods, J. R. Wallbank, M. Mucha-Kruczynski, B. A. Piot, P. M, I. V. Grigoreva, K. S. Novoselov, F. Guinea, V. I. Fal'ko, and A. K. Geim, Nature **497**, 594 (2013).

[21] A. Sandner, T. Preis, C. Schell, P. Giudici, K. Watanabe, T. Taniguchi, D. Weiss, and J. Eroms, Nano Letters **15**, 8402 (2015).

[22] R. Yagi, R. Sakakibara, R. Ebisuoka, J. Onishi, K. Watanabe, T. Taniguchi, and Y. Iye, Physical Review B **92**, 195406 (2015).

[23] D. Weiss, K. Klitzing, K. Ploog, and G. Weimann, EPL (Europhysics Letters) **8**, 179 (1989).

[24] R. Gerhardts, D. Weiss, and K. v. Klitzing, Physical Review Letters **62**, 1173 (1989).

[25] R. W. Winkler, J. P. Kotthaus, and K. Ploog, Physical Review Letters **62**, 1177 (1989).

[26] C. W. J. Beenakker, Physical Review Letters **62**, 2020 (1989).

[27] A. Matulis and F. M. Peeters, Physical Review B **75**, 125429 (2007).

[28] M. Tahir, K. Sabeeh, and A. MacKinnon, Journal of Physics: Condensed Matter **19**, 406226 (2007).

[29] K. S. Novoselov, A. K. Geim, S. V. Morozov, D. Jiang, M. I. Katsnelson, I. V. Grigorieva, S. V. Dubonos, and A. A. Firsov, Nature **438**, 197 (2005).

[30] Y. Zhang, Y.-W. Tan, H. Störmer, and P. Kim, Nature **438**, 201 (2005).

[31] V. V. Cheianov and V. I. Fal'ko, Phys. Rev. B **74**, 041403 (2006).

[32] M.-H. Liu, C. Gorini, and K. Richter, Physical Review Letters **118**, 066801 (2017).

[33] F. Pizzocchero, L. Gammelgaard, B. S. Jessen, J. M. Caridad, L. Wang, J. Hone, P. Bøggild, and T. J. Booth, Nature Communications **7** (2016).

[34] M. Drienovsky, A. Sandner, C. Baumgartner, M.-H. Liu, T. Taniguchi, K. Watanabe, K. Richter, D. Weiss, and J. Eroms, arXiv preprint arXiv:1703.05631 (2017).

[35] A. F. Young and P. Kim, Nat. Phys. **5**, 222 (2009).

[36] M. Drienovsky, F.-X. Schrettenbrunner, A. Sandner, D. Weiss, J. Eroms, M.-H. Liu, F. Tkatschenko, and K. Richter, Phys. Rev. B **89**, 115421 (2014).

[37] C. Handschin, P. Makk, P. Rickhaus, M.-H. Liu, K. Watanabe, T. Taniguchi, K. Richter, and C. Schönenberger, Nano Lett. **17 (1)**, 328 (2017).

[38] M.-H. Liu, Phys. Rev. B **87**, 125427 (2013).

[39] T. J. Thornton, M. L. Roukes, A. Scherer, and B. P. Van de Gaag, Physical Review Letters **63**, 2128 (1989).

[40] C. Beenakker and H. van Houten, Solid State Physics **44**, 1 (1991).

[41] S. Masubuchi, K. Iguchi, T. Yamaguchi, M. Onuki, M. Arai, K. Watanabe, T. Taniguchi, and T. Machida, Physical Review Letters **109**, 036601 (2012).

[42] F. M. Peeters and P. Vasilopoulos, Physical Review B **46**, 4667 (1992).

[43] A. D. Mirlin and P. Wölfle, Physical Review B **58**, 12986 (1998).

[44] P. H. Beton, P. C. Main, M. Davison, M. Dellow, R. P. Taylor, E. S. Alves, L. Eaves, S. P. Beaumont, and C. D. W. Wilkinson, Physical Review B **42**, 9689 (1990).

[45] M. Monteverde, C. Ojeda-Aristizabal, R. Weil, K. Bennaceur, M. Ferrier, S. Guéron, C. Glattli, H. Bouchiat, J. N. Fuchs, and D. L. Maslov, Physical Review Letters **104**, 126801 (2010).

[46] J. Heremans, B. K. Fuller, C. M. Thrush, and V. Bayot, Phys. Rev. B **54**, 2685 (1996).

[47] R. K. Kumar, D. A. Bandurin, F. M. D. Pellegrino, Y. Cao, A. Principi, H. Guo, G. H. Auton, M. B. Shalom, L. A. Ponomarenko, G. Falkovich, K. Watanabe, T. Taniguchi, I. V. Grigoreva, L. S. Levitov, M. Polini, and A. K. Geim, Nature Physics **4240** (2017).